Driving magnetic domains at the nanoscale by interfacial strain-induced proximity

Journal:	*Nanoscale*
Manuscript ID	NR-ART-11-2020-008253.R1
Article Type:	Paper
Date Submitted by the Author:	08-Feb-2021
Complete List of Authors:	Valmianski, Ilya; University of California at San Diego Fraile Rodriguez, Arantxa; Universitat de Barcelona, Física de la Matèria Condensada Rodríguez-Álvarez, Javier; Universitat de Barcelona, Física de la Matèria Condensada García del Muro, Montserrat; Universitat de Barcelona, Física de la Matèria Condensada Wolowiec, Christian; University of California at San Diego Kronast, Florian; Helmholtz-Zentrum Berlin, Ramirez, Juan Gabriel; Universidad de los Andes, Physics Schuller, Ivan K.; University of California at San Diego, Labarta, Amilcar; Universitat de Barcelona, Departament de Física de la Matèria Condensada i Institut de Nanociència Batlle, Xavier; Universitat de Barcelona, Departament de Física Fonamental and Institut de Nanociència i Nanotecnologia IN2UB

Driving magnetic domains at the nanoscale by interfacial strain-induced proximity

Received 00th January 20xx,
Accepted 00th January 20xx

DOI: 10.1039/x0xx00000x

Ilya Valmianski[a], *Arantxa Fraile Rodríguez*[b,c,]*, *Javier Rodríguez-Álvarez*[b,c], *Montserrat García del Muro*[b,c], *Christian Wolowiec*[a], *Florian Kronast*[d], *Juan Gabriel Ramírez*[e], *Ivan K. Schuller*[a], *Amílcar Labarta*[b,c], and *Xavier Batlle*[b,c]

We investigate the local nanoscale changes of the magnetic anisotropy of a Ni film subject to an inverse magnetostrictive effect by proximity to a V_2O_3 layer. Using temperature-dependent photoemission electron microscopy (PEEM) combined with X-ray magnetic circular dichroism (XMCD), direct images of the Ni spin alignment across the first-order structural phase transition (SPT) of V_2O_3 were obtained. We find an abrupt temperature-driven reorientation of the Ni magnetic domains across the SPT, which is associated with a large increase of the coercive field. Moreover, angular dependent ferromagnetic resonance (FMR) shows a remarkable change in the magnetic anisotropy of the Ni film across the SPT of V_2O_3. Micromagnetic simulations based on these results are in quantitative agreement with the PEEM data. Direct measurements of the lateral correlation length of the Ni domains from XMCD images show an increase of almost one order of magnitude at the SPT compared to room temperature, as well as a broad spatial distribution of the local transition temperatures, thus corroborating the phase coexistence of Ni anisotropies caused by the V_2O_3 SPT. We show that the rearrangement of the Ni domains is due to strain induced by the oxide layers' structural domains across the SPT. Our results illustrate the use of alternative hybrid systems to manipulate magnetic domains at the nanoscale, which allows for engineering of coercive fields for novel data storage architectures.

Introduction

Coupling between lattice degrees of freedom and the spin systems without the use of magnetic fields allows for efficient spintronic devices[1,2]. Typically, the coupling occurs via proximity effects in hybrid materials in which a multifunctional material is in contact with a magnetic one[1-5]. Such experiments often involve piezoelectric and ferromagnetic materials although there are several other methods to realize spin-lattice coupling such as ion manipulation (e.g. in shape memory alloys[3,4]), spin-orbit coupling[5], or lattice strain[6] . Via magnetoelastic effects, it is possible to change the overall magnetic anisotropy either in magnitude and/or direction, allowing for a control of the magnetic properties of the ferromagnetic layer using a bias voltage[7–11]. While piezoelectric systems allow for tuning the magnetic properties, the effects are generally small (Ref. 12 and references therein). A promising alternative to produce large effects uses materials which exhibit a first order structural phase transition (SPT)[13]. It is particularly interesting to develop devices in which the phase transition can be triggered by thermal, electrical[14], or optical[15] stimuli. Within this context, it has been demonstrated that the proximity of a ferromagnetic (FM) layer with an archetypal Mott vanadium oxide results in a dramatic modification of the magnetic properties across the vanadium oxide SPT due to interfacial stress[2,16,17]. In particular, for Ni/V_2O_3 bilayers, the V_2O_3 SPT can induce changes in the coercive field up to 500% due to the phase coexistence in the oxide layer across the SPT.[17]

V_2O_3 undergoes a monoclinic-rhombohedral SPT around 165 K with a volume change of 1.4%[18–20] that can be induced by temperature[18], pressure[18,21], or light. [22–24] It has been suggested that the inverse magnetoelastic effect at the Ni/V_2O_3 interface leads to a drastic reconfiguration of the domain size and magnetic pinning in the Ni layer[16,17]. However, the actual mechanism governing this effect has only been addressed indirectly by micromagnetic simulations[17]. Direct measurements of the local magnetic domain reconfiguration across the V_2O_3 SPT are still lacking. In addition to its fundamental interest, direct observations of the strain-induced magnetic domains across the SPT are highly relevant since controlling the domain energy landscape and the magnetic correlation length at the nanoscale may lead to novel data storage architectures (Ref. 1 and references therein).

Here we have investigated the local nanoscale changes in the magnetic anisotropy of Ni/V_2O_3 layers, fabricated similarly to

---

[a] Department of Physics and Center for Advanced Nanoscience, University of California San Diego, La Jolla, CA 92093, USA.
[b] Departament de Física de la Matèria Condensada, Universitat de Barcelona, 08028 Barcelona, Spain
[c] Institut de Nanociència i Nanotecnologia (IN2UB), Universitat de Barcelona, 08028 Barcelona, Spain
*Corresponding author: arantxa.fraile@ub.edu
[d] Helmholtz-Zentrum Berlin für Materialien und Energie GmbH, 12489 Berlin, Germany
[e] Department of Physics, Universidad de los Andes, Bogotá 111711, Colombia.
*Corresponding author, E-mail: arantxa.fraile@ub.edu
Electronic Supplementary Information (ESI) available. See DOI: 10.1039/x0xx00000x

those in Refs. 17 and 25 using a combination of X-ray magnetic circular dichroism (XMCD) and photoemission electron microscopy (PEEM) to image the local Ni domain patterns, together with macroscopic anisotropies determined by magnetometry and ferromagnetic resonance (FMR). We find that the Ni layer magnetic domain reconfiguration (domain size and correlation length) across the V_2O_3 SPT is responsible for the large coercive field increase. Furthermore, the changes in magnitude and direction of the magnetic anisotropy are strongly correlated with the structural transformations undergone by V_2O_3 and are supported by angular dependent FMR and magnetometry measurements. In addition, micromagnetic simulations based on the change in the magnetic anisotropy agree with the PEEM data. This opens the possibility of manipulating the nanoscale magnetic domains of a ferromagnetic layer using the strain produced by an oxide layer undergoing an externally driven SPT.

In a wider context, it is also worth highlighting that, associated with the SPT, vanadium oxides undergo a characteristic metal-insulator transition (MIT)[26] involving changes of several orders of magnitude in the electrical resistivity[27,28] and significant changes of the optical properties at all wavelengths under thermal excitations[29]. These characteristics make vanadium oxide an active component of photoelectric hybrid materials such as tunable terahertz metamaterial absorbers[30]. In combination with a proximal magnetic layer, vanadium oxide provides an additional degree of freedom for the design of hybrid functional materials combining the advantages of *straintronics*[31] and opto-electronic devices.

Results and discussion

Sample fabrication and characterizations

The Ni (10 nm)/V_2O_3 (100 nm) heterostructures were prepared by high-vacuum magnetron sputtering deposition with a base pressure of 10^{-7} Torr. The V_2O_3 films were deposited at 750 ºC in 4 mTorr of ultrahigh purity Ar by rf-sputtering at 100 W of a V_2O_3 target on r-plane (012) sapphire (α-Al_2O_3) substrates, as described earlier [16]. The V_2O_3 films were cooled to 300 K prior to Ni deposition to improve film smoothness. After recovering

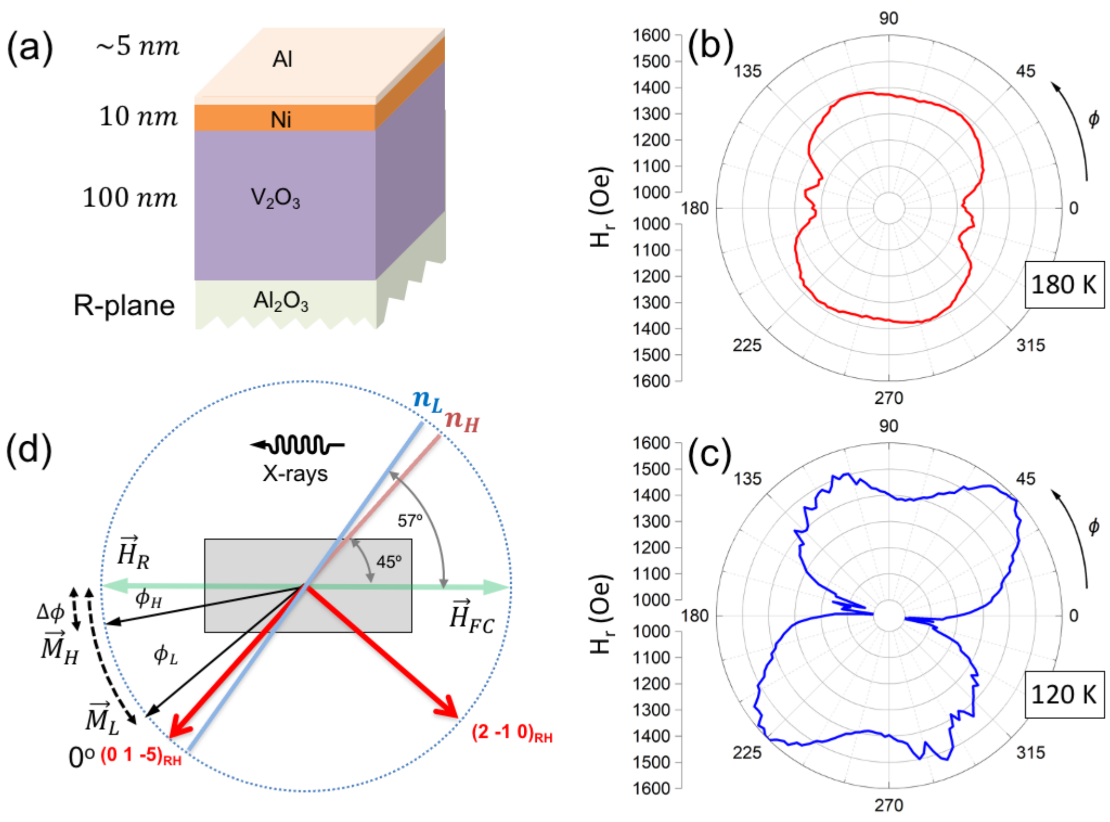

Fig. 1 (a) Schematic illustration of the samples showing the nominal thickness of the layers composing the heterostructure. (b) Polar plots of the ferromagnetic resonance (FMR) fields H_r above the structural phase transition (SPT) at 180 K in Ni/V_2O_3 and (c) below the SPT at 120 K. The initial 0º angle is set along the $(0\ 1\ \text{-}5)_{RH}$ direction. The easy axes correspond to the global minima in the resonance field H_r. The hard axes correspond to global maxima in H_r. Note the emergence of a secondary easy axis at 77º (255º) in panel (c) and a roughly 32º-35º shift in the hard axis upon cooling through the SPT. (d) Orientation of the sample with respect to V_2O_3 $(0\ 1\ \text{-}5)_{RH}$ and $(2\ \text{-}1\ 0)_{RH}$ crystallographic directions (red lines), the applied magnetic fields (green lines), and the projection of the X-ray wave vector on the sample surface. Light brown and blue solid straight lines indicate the high- and low-temperature anisotropy axes, n_H and n_L, respectively. The expected orientations of the high- and low-temperature Ni magnetizations, $\vec{M}_H$ and $\vec{M}_L$, are also depicted. $\Delta\phi$ indicates the average value of $\vec{M}_H$ and $\vec{M}_L$ rotation with respect to the applied magnetic fields.

the base pressure, the Ni layer was deposited at 300 K by rf sputtering from a Ni target. A nominal 5 nm-thick Al cap layer was deposited to prevent oxidation. A schematic illustration of the heterostructure is shown in Fig. 1a. The X-ray characterization, including X-ray reflectivity (XRR) for thickness measurements and X-ray diffraction (XRD) for structural characterization, was carried out using a Rigaku Smartlab Diffractometer. XRD measurements show that the V_2O_3 films were epitaxial following the substrate directions as previously found in similarly prepared films.[16,32,33] The low-temperature phase of V_2O_3 splits into a mosaic of two distinct crystallites, with an average size of 8 nm, randomly distributed throughout the film as shown in Ref. [32] The Ni films are textured with the (111) axis perpendicular to the film surface and the roughness at the Ni/V_2O_3 interface is ~ 2 nm. Due to the morphology of the terraced sapphire substrate, long-range rips and localized voids oriented along the V_2O_3 (0 1 -5) diffraction vector appear in the microstructure, which induce an effective uniaxial magnetic anisotropy in the Ni film.[32] The rips and voids are of approximately 15 nm in width and lengths ranging from 30 nm to several hundred nm. As a result, in the Ni/V_2O_3 bilayer, a ribbon-like microstructure shows up in the Ni layer, yielding contiguous regions of about 100 nm in width and more than 500 nm in length.[32]

The Ni and V_2O_3 layers were further characterized by Near-Edge X-ray Absorption Spectroscopy (NEXAFS), performed at the UE49 SPEEM beamline at the BESSY II synchrotron facility of the Helmholtz-Zentrum Berlin (HZB)[34,35]. The metallic character of the Ni layer is confirmed by both the presence of the expected satellite peak at about 6 eV above the L_3 edge and the absence of oxide-related multiplet features around the $L_{3,2}$ edges (Fig. S1a in the Supporting Information). As for the V_2O_3, the NEXAFS spectra, recorded in the insulating, low-temperature phase (150 K), show the usual two main peaks at the energies corresponding to the L_3 and L_2 edges[36] (Fig. S1b in Supporting Information).

Global static and dynamic magnetic measurements

In-plane angular-dependent ferromagnetic resonance (FMR) experiments were performed as a function of temperature both above and below the SPT temperature of V_2O_3 at 150 K (Fig. 1b and 1c and Fig. S2 in the Supporting Information). In the high-temperature, metallic phase of V_2O_3, there is an *effective* uniaxial anisotropy in the Ni layer with the easy axis along the (0 1 -5) direction of the rhombohedral phase (RH)[32]. Thus, the sample was positioned in the resonant cavity so that the (0 1 -5)$_{RH}$ direction corresponds to the initial angle of 0° (Fig. 1d). The effective easy and hard axes at approximately 0° (or 175°) and 85° (or 265°), respectively, are identified in the FMR polar plots (Fig. 1b and 1c) by the global minima and maxima in the resonance field, H_r, at which they occur. Furthermore, the effective magnetic anisotropy in the Ni layer changes abruptly through the V_2O_3 SPT. The anisotropy energy is much higher in the low-temperature monoclinic V_2O_3 phase and lower in the high-temperature rhombohedral phase, as evidenced by the sharp increase in the coercivity. In addition, below the SPT, in the insulating phase of V_2O_3, there is a slight rotation in the anisotropy axes in the Ni layer (see for comparison Fig. 1b at 180 K and Fig. 1c at 120 K). For example, the FMR polar plot at 120 K reveals an average -12° rotation in the easy axis from 0° (175°) at high temperature to -12° (163°) at low temperature, as well as the emergence of two new, low-temperature hard axes at about 117° (300°) and 45° (225°). The average value of -12° for the angular rotation of the effective easy axis is found as the mean value of the two minima at about -7° and -15° in the polar plot shown in Fig. 1c. Consequently, the high-temperature easy axis about the (0 1 -5)$_{RH}$ direction at 0° (175°) still persists down to low temperature, but showing significant enhancements in both its uniaxial character (compare the shape of the polar plots in Fig. 1b and Fig. 1c) and the magnitude of the effective anisotropy. Moreover, there is a secondary easy axis at 77° (255°) but with a corresponding anisotropy energy much smaller than that for the easy axis at -12° (163°). Therefore, as a first approximation, we can neglect the effect of this secondary easy axis and assume that the effective magnetic anisotropy in the Ni layer is still uniaxial at low temperature along a direction at about -12° (163°). However, it is worth stressing that the ~32º–40º shift in the hard axes and the emergence of an additional easy axis suggest that there is a departure from a *true* uniaxial anisotropy in the Ni layer upon cooling through the SPT into the insulating phase of V_2O_3. This is further suggested by the fact that the angular dependences of the coercive field at several temperatures across the SPT show much a smaller variation than those expected from the Stoner Wohlfarth model for a system with uniaxial anisotropy (see Fig. 4 in Ref. 32. Fig. 1d shows a schematic for the definition of the low- and high-temperature, effective, uniaxial anisotropy easy axes, n_L and n_H, respectively, within this simplified model.

The *effective* uniaxial anisotropy in the Ni layer at high temperature is induced by the strain caused by the V_2O_3 microstructural terracing along the (0 1 -5)$_{RH}$ direction in the high-temperature phase of V_2O_3. Yet, the anisotropy energy profile in the Ni layer at low temperature stems from the emergence of additional strain in the low-temperature monoclinic phase of V_2O_3. Indeed, this may result from the combination of a strain along the (0 1 -5)$_{RH}$ direction – coincident with the high-temperature easy axis, n_H,– and another twin strain perpendicular to the (0 1 -5)$_{RH}$ direction, i.e., along the (2 -1 0)$_{RH}$ direction of the rhombohedral phase, see Fig. 1d.[37] The competition between those two strain directions thus results in the emergence of an effective, uniaxial-like anisotropy axis, n_L, which is shifted by -12º with respect to the (0 1 -5) $_{RH}$ direction, suggesting that the strain along the (0 1 -5)$_{RH}$ direction is still dominant at low temperature. It is also worth noting that even though two hard anisotropy axes at low temperature can be distinguished from FMR, the anisotropy energy associated with the hard axis oriented at 45° (225°) is stronger than that for the hard axis at 117° (300°), as inferred from the FMR intensity in Fig. 1c and Fig. S2 in the Supporting Information. This suggests a smaller magnetoelastic coupling between V_2O_3 and the Ni layer at the 117° (300°) direction and, consequently, a low-temperature, effective uniaxial-like anisotropy.

To summarize this part, the complex strain transferred at low- and high-temperature by the V_2O_3 to the Ni layer, does not imprint a *true* uniaxial anisotropy in the Ni layer, as shown by the angular dependences of the FMR in Fig. 1b and 1c. However, to gain an overall idea of how the Ni magnetization rotates across the SPT, it is worthwhile to approximate the anisotropy energy in the Ni layer, both at the high-temperature and low-temperature phases of V_2O_3, by effective uniaxial axes at 0° (175°) (along the (0 1 -5)$_{RH}$ direction) and at -12° (163°), respectively. Note also that a micromagnetic model based on this effective uniaxial approximation of the anisotropy energy for the low-temperature phase reflects well the rotation of the Ni magnetization across the SPT, as will be discussed later.

Magnetic field and temperature-dependent magnetization data were obtained with a field step of 5 Oe and at a slow sweep rate (1–2 K/min), to minimize thermal lag and obtain reproducible measurements across the V_2O_3 SPT. Figure S3 in the Supporting Information shows hysteresis loops at selected temperatures across the V_2O_3 transition with the magnetization normalized by the Ni volume. Data were collected with the magnetic field applied along the long axis of the sample, i.e. a direction forming a 45° angle with n_H ((0 1 -5)$_{RH}$ direction) (see Fig. 1d). Figure S3 in the Supporting Information shows symmetric, ferromagnetic hysteresis loops with a sharp rise of their coercive field, H_c, across the V_2O_3 SPT, consistent with previous findings on similar bilayers.[16,33] The temperature dependence of H_c is shown in Fig. 2. During cooling from 300 K, a maximum of $H_c = 320$ Oe is found at 155 K, which is about four times the value at 300 K (H_c(200K) ~ 85 Oe) which remains almost constant down to 120 K independent of the temperature sweep direction. For extremely smooth Ni/V_2O_3 interfaces, in addition to the four-fold increase, the coercive field has a superimposed sharp, narrow peak at the transition temperature (~155K) [17], which is barely visible in Fig. 2. For this paper, the above mentioned ribbon-like Ni microstructure[32] hinders the occurrence of a smooth Ni/V_2O_3 interface. The temperature corresponding to the maximum of the H_c is shifted by about 7 K to higher temperatures during heating (not shown), which is consistent with the thermal hysteresis observed for the V_2O_3 first order SPT.[26]

In addition, a minimum in the saturation magnetization (M_s) is observed at the same temperature at which the maximum H_c is found (not shown). Such large and reproducible changes in both H_c and M_s coincide with the onset of the V_2O_3 phase transition[16,17] and are thus likely triggered by the structural changes across the SPT. The 1.4% volume change across the V_2O_3 SPT[18–20] produces stress in the Ni overlayer. In turn, the stress in the Ni layer changes the magnetic properties by an inverse magnetostrictive effect.[38] This interfacial magnetoelastic coupling shows up either with an applied field or in remanence.[16] The magnetization curves overlap with thermal cycling, indicating the reproducibility of the process.[16]

It should be noted that, because the V_2O_3 film has a roughness of about 2 nm and the Ni film is thin and polycrystalline, the strain induced in the Ni cannot be inferred from the Ni Bragg peaks from a standard, lab-based XRD measurement.[16,37] However, a rough estimate was done in Ref. 16 on similar samples, assuming that a uniform strain in the Ni layer causes the coercivity changes due to the stress anisotropy energy, and obtained similar values (σ =553 MPa) than for the strain reported in V_2O_3.[16]

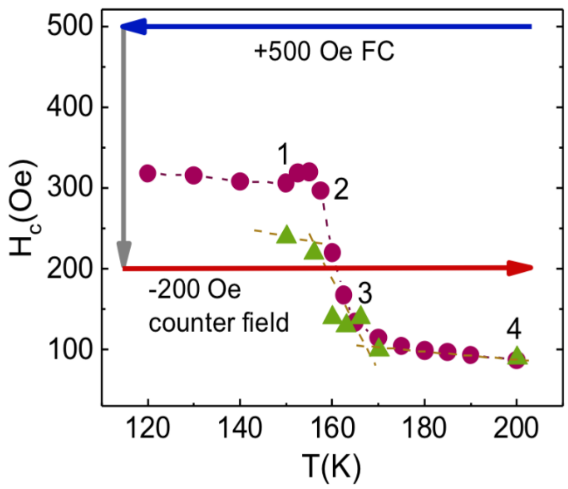

Fig. 2 Coercivity as a function of temperature of Ni(10 nm)/V_2O_3(100 nm) across the V_2O_3 structural phase transition recorded while cooling the sample from 300 K to 120 K (only data from 200 K are shown). A sharp rise in the coercive field, H_c, of about a factor of four, is found as the temperature goes below the V_2O_3 SPT. The arrows refer to the experimental protocol prior to acquiring the XMCD-PEEM images (see text and Fig. 3). The numbers refer to the XMCD-PEEM images at the corresponding temperatures (150 K, 163 K, 170 K, 200 K) in Fig. 3. The garnet dots represent the coercivity values obtained from the experimental loops while the green triangles correspond to those obtained from micromagnetic simulations, as discussed later. The error bars are smaller than the data point symbols.

The effective uniaxial anisotropy field H_H induced in the Ni layer by the high temperature V_2O_3 phase (at around 200 K) is estimated to be about twice the coercive field. Since the coercive field was measured with the field applied 45º off the easy axis, H_H ~ 170 Oe, assuming the Stoner Wohlfarth model and an effective uniaxial anisotropy. The low-temperature anisotropy field, H_L, close to 120 K is thus estimated to be of the order of H_L ~ [H_c(120 K)/H_c(200 K)] H_H ~ 600 Oe. These values of the anisotropy fields will be used later in the micromagnetic simulations to study the rotation of the Ni magnetization across the SPT.

Imaging of magnetic domain configurations

Direct imaging of the Ni domain structure as a function of the temperature was performed using PEEM[39] and exploiting the XMCD effect as magnetic contrast mechanism[40]. PEEM measurements were carried out at the UE49 SPEEM beamline at the BESSY II synchrotron facility of the Helmholtz-Zentrum Berlin (HZB).[34,35] XMCD images reflect the projection of the local magnetization on the photon propagation vector of the impinging X-rays according to $I(C^{\pm}) = I_0 \pm \gamma(\vec{k} \cdot \vec{m})$, where $C^{\pm}$ denotes right- and left-handed circular polarization, I_0 is the isotropic (non-magnetic) contribution, $\vec{k}$ is the X-ray propagation vector with an angle of incidence $\theta_k = 16°$ with respect to the surface of the sample, $\vec{m}$, is the magnetization vector, and γ is a material- and photon energy-dependent constant. The projection of $\vec{k}$ onto the sample surface was aligned parallel to the in-plane projection of the (-1 0 4)$_{RH}$ crystallographic direction of V_2O_3 (long axis of the sample), which is at 45° with respect to the high-temperature Ni easy axis, n_H, and at 57° to the low-temperature easy axis, n_L (see Fig. 1d).

The initial magnetic state of the sample was established by saturating the Ni layer at 296 K with an *in-situ* magnetic field of H =1 kOe applied along the long axis of the sample (Fig. 1d). Subsequently, the magnetic field was reduced to H_{FC}=500 Oe and the samples were field cooled (FC) through the V_2O_3 SPT down to 130 K at a temperature rate of 2-3 K/min. The direction of H_{FC} during cooling was always along the long axis of the sample (i.e., parallel to the in-plane projection of the X-ray propagation vector, $\vec{k}$), while the magnitude of H_{FC} was well above the high-temperature anisotropy field, H_H ~ 170 Oe. This procedure (shown in Fig. 1d and schematically outlined by arrows in Fig. 2) ensured that the Ni film was uniformly magnetized at high temperature. Then, at the lowest measuring temperature of about 140 K, the direction of the magnetic field was reversed along the long axis of the sample (in-plane projection of $\vec{k}$) and was kept constant at a reversed field, H_R = 200 Oe. This value of H_R is less than H_L in the low-temperature state (H_L ~ 600 Oe) but larger than H_H in the high-temperature state (Fig. 2). It therefore induces a progressive rotation of the Ni magnetization from a direction close to the anisotropy axis at low temperature towards the field direction at high temperature, as will be shown in the following.

Next, we collected stacks of XMCD images under H_R at selected temperatures while warming across the V_2O_3 SPT. Magnetic domain contrast was obtained by the pixel-wise intensity asymmetry ratio of two PEEM images sequentially recorded with $C^{\pm}$ polarization, $[I(C^{+})-I(C^{-})]/[I(C^{+})+I(C^{-})]$, at the resonant L_3 absorption edge of Ni (851.7 eV). The XMCD intensity is proportional to the cosine of the azimuthal angle ϕ between the magnetization and the X-ray propagation vector $\vec{k}$. Thus, the local magnetization direction can be directly extracted from the evaluation of the XMCD intensities. Note, however, that PEEM data recorded at a fixed ϕ is insensitive to the sign of the angle between the Ni magnetization and the field direction. As a consequence, symmetric orientations of the Ni magnetization at both sides of $\vec{H}_R$ appear with the same color in the XMCD images. In these magnetization maps, the domains exhibit a color contrast ranging from blue to yellow, depending on the projection of the domain magnetization onto $\vec{k}$ (see Fig. 3). The blue regions represent the high-anisotropy, low-temperature Ni domains, while the yellow regions represent the low- anisotropy, high-temperature Ni domains. A typical measurement sequence consisted of an average of 20 individual PEEM images per $C^{\pm}$ polarization with an acquisition time of 5s each. This sequence was then corrected for sample drifts and then averaged to yield XMCD contrast images such as those shown in Fig. 3. The spatial resolution of our X-PEEM experiments is limited to about 30 nm. Figure 3 (top panels) show representative XMCD images recorded in the low-temperature (150 K) and high-temperature (200 K) states, as well as at temperatures across the SPT (163 K, 170 K). The corresponding points at these temperatures (150 K, 163 K, 170 K, and 200 K) in the macroscopic magnetometry measurements

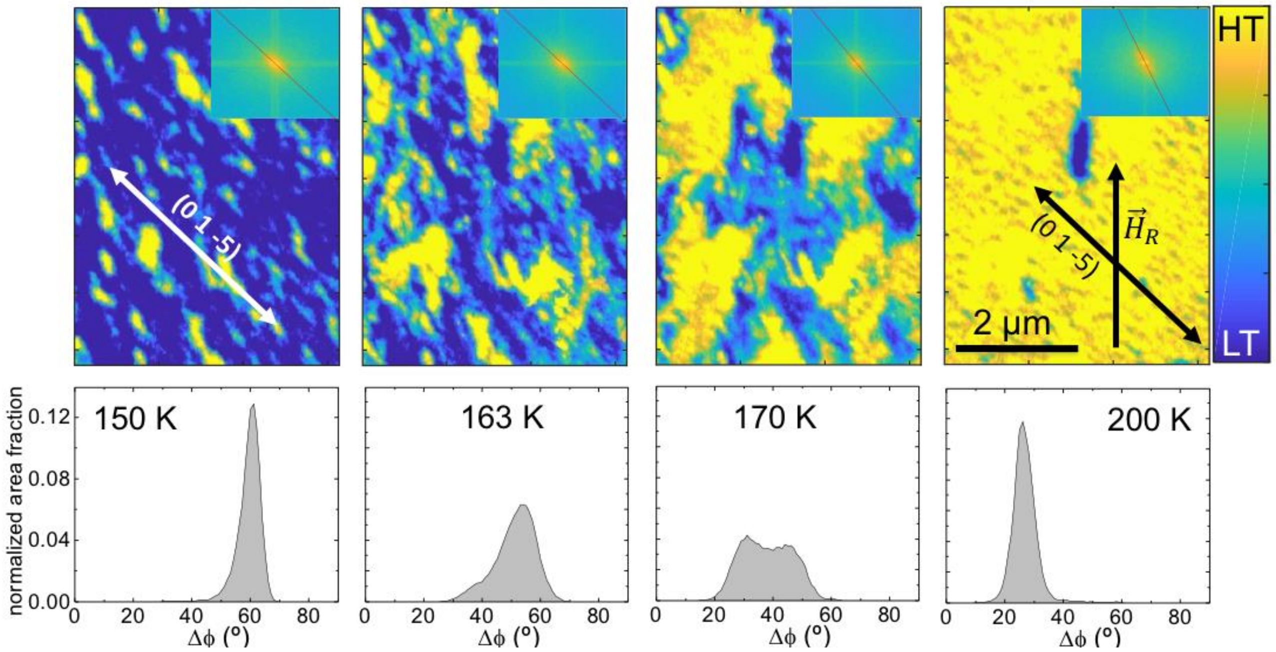

Fig. 3 Top row panels show representative XMCD-PEEM images recorded at temperatures below (150 K), across (163 K, 170 K) and above (200 K) the SPT of V_2O_3. The insets show their Fourier transforms. The initial state (blue contrast) at low temperature (LT) splits into a pattern of small domains (yellow) which progressively rotate and grow across the V_2O_3 SPT as the high-temperature (HT) phase is reached. Bottom row panels show histograms of the absolute value of the average rotation angle of the Ni magnetization with respect to the projection of the X-ray propagation vector on the sample surface, $\Delta\phi$, at selected temperatures (calculated from the images in the top row). Sharp $\Delta\phi$ distributions are found for the LT (150 K) and HT (200 K) phases in contrast to broader distributions in the middle of the V_2O_3 SPT (163 K, 170 K).

(Fig. 2), are labeled with numbers (1, 2, 3, and 4). It is found that while warming up across the V_2O_3 SPT, the initially almost saturated ferromagnetic state at low temperature (150 K) splits into a pattern of small domains, which progressively coalesce and rotate towards the field direction.

Figure 3 (top panels) unambiguously shows that ripple-shaped domains of about 100 nm in width and up to a few hundred nm in length are found in the Ni layer at all temperatures. This is consistent with the typical size of the low-temperature structural domains of V_2O_3 of about 100 nm and the characteristic isotropic length scale of electronic domains in the range of 100 to 400 nm)[25]. The long-range ordering of the Ni domains is also supported by the elliptical shape of the Fourier transform of the XMCD images (see insets in Fig. 3) whose tilting angle indicates the average orientation of the minority Ni domains at each temperature. The orientation of the Ni ripple domains matches well with that of the rips and voids in the V_2O_3 microstructure along the $(0\ 1\ \text{-}5)_{RH}$ vector.[32] At low temperature, although there is an emergent strain along the $(2\ \text{-}1\ 0)_{RH}$ direction lying perpendicular to the $(0\ 1\ \text{-}5)_{RH}$ direction[37] (see Fig. 1d), the ripple structure in the Ni layer is still present (Fig. 3, top panels), as also suggested in Ref. 32.

The full thermal cycle was repeated twice in the same area and in different areas of the sample to ensure reproducibility. In all cases, stochastic domain nucleation was found between thermal cycles with no appreciable defects acting as pinning sites. Stacks of XMCD images were also recorded during the cooling cycles (not shown). Reversible domain pattern characteristics were found between heating and cooling cycles, as well as thermal hysteresis of about 7 K, in agreement with the macroscopic magnetic measurements[16,17] (not shown).

Top panels in Fig. 3 also reveal that the magnetization rotation occurs progressively, with most of the magnetic layer transitioning through intermediate magnetization orientations as the temperature is scanned across the SPT due to the coexistence of the corundum and monoclinic phases of V_2O_3. It is worth stressing that, at low temperature, after applying $\vec{H}_R$, the Ni magnetization tends to lie at an angle ϕ_L close to the direction of the low-temperature easy axis n_L (Fig. 1d) since H_L is about three times greater than H_R. As the temperature is increased across the SPT, the Ni magnetization progressively rotates towards $\vec{H}_R$ since, for the high-temperature phase, $H_H < H_R$. Finally, at high temperature, the Ni magnetization points at a small angle ϕ_H with respect to $\vec{H}_R$ (Fig. 1d). Note that the XMCD contrast in these measurements is similar regardless of the sign of these angles. In addition, there is an intrinsic uncertainty of about 5-10° in the determination of ϕ from XMCD data, due to the relative misalignment in either the sample positioning or the magnetic field axis with respect to the projection of $\vec{k}$ on the sample surface. Consequently, $\Delta\phi$, defined as the absolute value of the rotation angle with respect to an arbitrary direction (that of the projection of $\vec{k}$ on the sample surface) close to the long axis of the sample (Fig. 1d), is the actual magnitude we analyzed.

Bottom row panels in Fig. 3 show histograms of $\Delta\phi$ calculated from the images displayed in the top row panels at selected temperatures. The histograms indicate sharp distributions with values of the standard deviation of about 3-5° for the low-temperature (150 K) and high-temperature (200 K) phases, and broader distributions of intermediate orientations across the SPT (163, 170 K), with a standard deviation within 8-10° (Fig. 4b), suggesting that the magnetization rotation is induced by the V_2O_3 SPT.

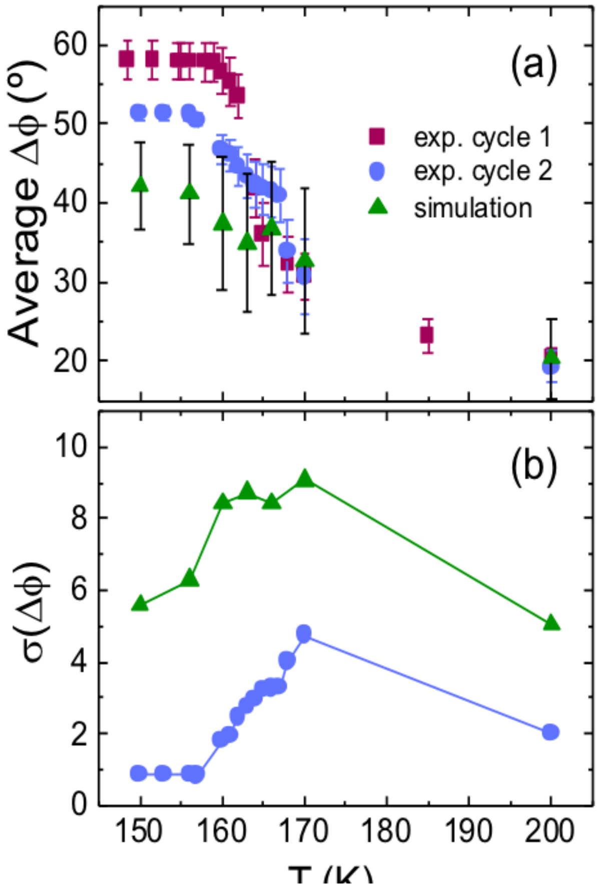

Fig. 4 a) Average rotation angle of the Ni magnetization, $\Delta\phi$, as a function of the temperature. Experimental data from XMCD images are plotted as solid garnet squares (cycle 1) and solid blue circles (cycle 2). Data from micromagnetic simulations are plotted as green triangles. (b) Standard deviation of the histograms of $\Delta\phi$ as a function of the temperature for the experimental cycle 2 (solid blue circles) and micromagnetic simulations (solid green triangles).

The temperature dependence of the average value of $\Delta\phi$ is shown in Fig. 4a for two consecutive thermal cycles performed in the same area of the sample following the same experimental protocol. The XMCD images for the second run are shown in Fig. S4 in the Supporting Information. Both runs show a consistent transition occurring around 165 K, in agreement with the macroscopic magnetic measurements (Fig. 2). The overall reorientation of the Ni magnetization across the SPT shows an average rotation of 30-35° from $\vec{M}_L$ to $\vec{M}_H$ (ϕ_L to ϕ_H) (see Fig. 1d). This average rotation is comparable with the results computed applying the Stoner Wohlfarth model to the anisotropy energy scheme depicted in Fig. 1d for $H_L \sim 600$ Oe and $H_H \sim 170$ Oe as estimated from $H_c(T)$ in Fig. 2. From these calculations, $\vec{M}_L$ points along $\phi_L \sim 44°$ counter-clockwise from $\vec{H}_R$, while $\vec{M}_H$ points along $\phi_H \sim 20°$ counter-clockwise from $\vec{H}_R$ (see Fig. 1d). This gives rise to an average $\Delta\phi \sim 24°$, in agreement with the 30-35° average rotation found from XMCD, considering the above-mentioned intrinsic uncertainty of about 5-10° in the determination of ϕ.

Note that the minor disagreement in the initial magnetization between the two cycles in Fig. 4a is possibly related to slightly different initial magnetic states of the Ni layer. Furthermore, the spread in the magnetization distribution (Fig. 4b), determined from the standard deviation of $\Delta\phi$ in the bottom panels in Fig. 3, progressively grows with increasing temperature and reaches a maximum at a similar temperature to which both the 50% areal fill fraction of the low-temperature phase and 50% fill fraction of the high-temperature structural V_2O_3 phase are reached.[25] This is clear evidence that the reorientations of the magnetic moments are due to the lattice deformation of the Ni. This is associated with the stress caused by the coexistence of the low- (monoclinic) and high- (corundum) temperature phases in V_2O_3 at the SPT, which are transferred to the magnetostrictive Ni layer by a strong elastic coupling at the interface. It should also be noted that the stress relief at grain boundaries may play a predominant role, as it does for instance in artificial multiferroic heterostructures.[41,42]

Micromagnetic simulations

In order to get a deeper insight into the magnetic domain formation, we performed micromagnetic simulations using the OOMMF[43] code. We model the Ni layer with a 10μm x10μm x10 nm layer with a uniform exchange constant of $A = 3.4\cdot10^{-7}$ erg/cm and a saturation magnetization of $M_s = 494$ emu/cm³.[44] For the simulations, the Ni layer was discretized into a mesh of 100 x 100 x10 nm³ cells over the whole simulated area of 10 x 10 μm². The cell size was of the order of the Ni grain size, as observed by AFM on similar samples[17], and comparable to the pixel size from both PEEM (Fig. 3) and Scanning Near-field Optical Microscopy (SNOM) measurements.[25] The simulated area was also comparable to the size of the XMCD images (Fig. 3). Accordingly, a direct comparison with the experimental domain configurations can be performed.

In addition, one of the two uniaxial anisotropies along the axes n_L and n_H with respective values of $H_L \sim 600$ Oe and $H_H \sim 170$ Oe for the low- and high-temperature phases, as estimated in section II, were assigned to each of the cells to simulate the effect on the Ni layer of the coexistence of structural domains undergoing the SPT.[25,37] These domains were simulated in the Ni layer as a random distribution of rectangular 500 nm x 700 nm regions, tilted 45° off the x-axis (parallel to the magnetic field direction) to reproduce the shape of the Ni domains in the XMCD images in Fig. 3. At each simulated temperature, both the area fraction covered by the rectangular domains and the type of uniaxial anisotropy were set to match those of the minority Ni domains in the corresponding XMCD image. The rest of the Ni cells were set to the uniaxial anisotropy corresponding to the

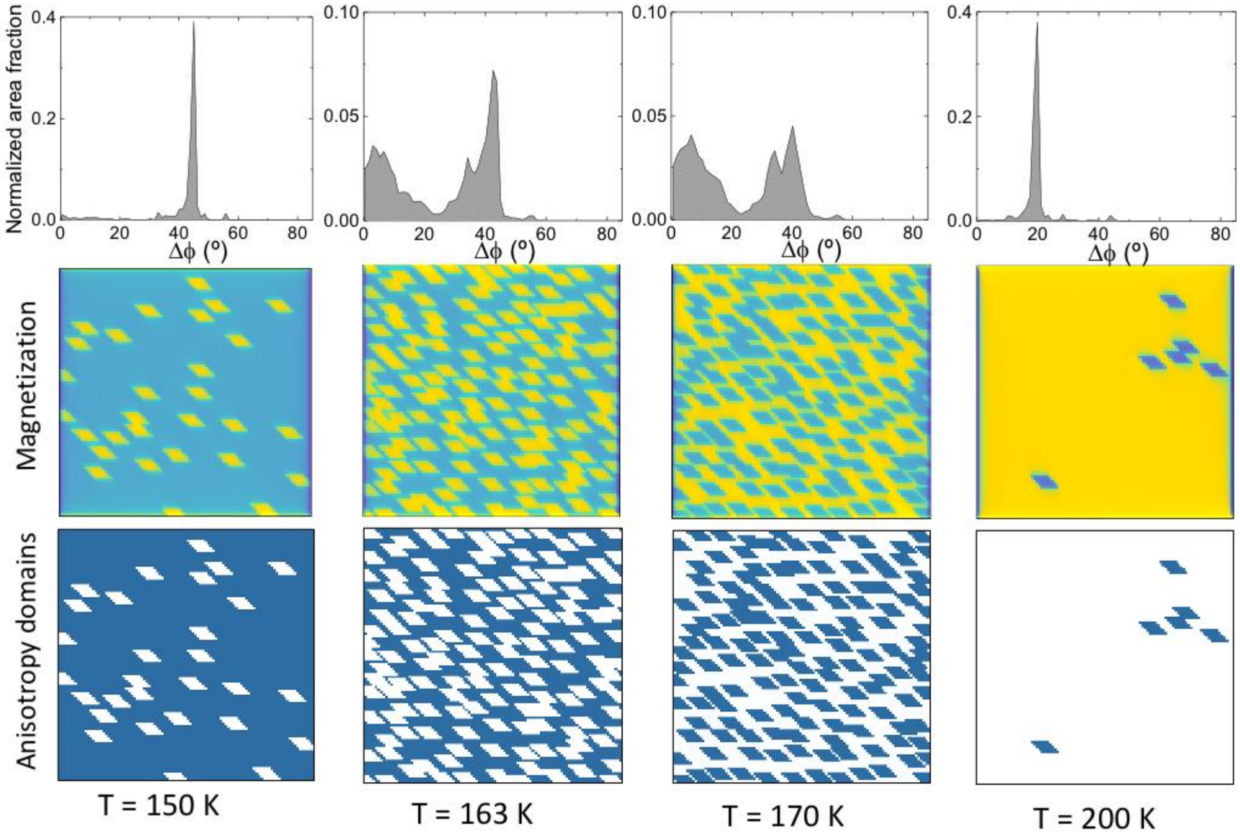

Fig. 5 Results of micromagnetic simulations as a function of the temperature showing (top panels) histograms of the average rotation angle of the Ni magnetization, $\Delta\phi$, and spatial distributions of both the magnetization angle (middle panels) and the anisotropy domains (bottom panels). In the middle row panels, the regions with orientations of the Ni magnetization corresponding to the high- and low-temperature phases are indicated by yellow and blue colors, respectively. In the bottom row panels, the regions with low- and high-temperature anisotropies are indicated with blue and white colors, respectively. The remarkable agreement between the middle and bottom row panels for each temperature is a good indication of how well such a simple micromagnetic model captures the essence of the magnetization reorientation across the V_2O_3 SPT.

majority phase. Therefore, the temperature was mapped into the simulations by mimicking the experimental configurations of anisotropy domains obtained from the XMCD images.

To reproduce the experimental PEEM conditions in our simulations, a 200 Oe uniform magnetic field was applied to the Ni layer in the opposite direction to the initial saturated state, allowing the Ni magnetization to reach a stationary state. The final configuration of cell magnetizations was greatly influenced by the competing anisotropies introduced to simulate the proximity with the V_2O_3. The bottom row panels in Fig. 5 show the configurations of high- and low-anisotropy domains in the Ni layer at each simulated temperature across the SPT. The middle row panels show the corresponding results for the magnetization configurations, while the top row panels display the histograms of $\Delta\phi$, defined as in the XMCD images. In the middle row panels in Fig. 5, the blue regions represent the high-anisotropy, low-temperature Ni domains, while the yellow regions represent the low- anisotropy, high-temperature Ni domains. The agreement with the corresponding PEEM measurements shown in Fig. 3 is remarkable. Furthermore, the temperature dependence of both the average value of $\Delta\phi$ (Fig. 4a) and the corresponding standard deviation $\sigma(\Delta\phi)$ (Fig. 4b), show a good correspondence with the values obtained from PEEM. In particular, $\sigma(\Delta\phi)$ is small both at low and high temperatures and reaches a maximum at the transition temperature (about 165 K), a signature of the phase coexistence across the transition.

We also performed a second set of simulations where the distribution of low/high anisotropy domains is done according to the spatial conductivity pattern in V_2O_3 taken from the SNOM images in Fig. 4 of Ref. [25]. The results, shown in Fig. S5 in the Supporting Information, show a high resemblance between the spatial patterns of the simulated local Ni magnetization and the experimental V_2O_3 conductivity at the same temperatures[21] as well as with the electro-thermal filaments observed by optical reflectivity during V_2O_3 resistive switching.[45]

In summary, a simple micromagnetic model based on the competition between two effective uniaxial-like anisotropy axes for the high-temperature and low-temperature phases reproduces well the observed local and global experimental features across the V_2O_3 SPT.

Domain correlation lengths and spatial Ni map of the SPT temperatures

We determined the evolution of the lateral correlation length of the rotated Ni domains imprinted by the V_2O_3 across the SPT using a radial distribution function analysis. For each XMCD image within the whole temperature-dependent image stack we calculated the radial average of the pair correlation of all pairs of bright pixels as a function of the distance between them (yellow pixels in Fig. 3). Such a pair correlation function is related to the probability of finding a bright pixel at a given distance from another bright pixel. The resulting pair correlation curves (see Fig. S6 in the Supporting Information) fit well to a single exponential decay from which the domain correlation lengths are directly obtained. Figure 6a shows an increase of the Ni domain correlation length ranging from 0.75 μm in the high temperature phase to 1.5 μm in the low temperature phase, and reaching a maximum of 2.25 μm at ~165 K, the temperature at which the largest phase coexistence is found (see Fig. 3 for comparison). This behavior resembles the universal scaling of temperature-dependent spatial correlations near a critical point[46], and is in agreement with both the structural correlation length associated with the structural phase coexistence and with the electronic correlation length originating from the metal-insulator V_2O_3 domains[25]. In our case, the increase and the peak in the Ni domain correlation length near the SPT are good indicators of the tendency of Ni to break into a magnetic microstructure with a characteristic length scale resembling the characteristic stripes of the underlying V_2O_3 structural domains.[25] The Ni domain correlation length reaches its maximum at a value a few times larger than the correlation length associated with the metallic V_2O_3 domains (around 400 nm)[25] and are about 50% larger than the maximum of the V_2O_3 structural correlation length (about 1.5 μm).

The fact that the correlation length of the magnetic domains is larger than the underlying V_2O_3 structural domains is not surprising. The Ni domain configuration is given by the balance between two main contributions. The energetic preference of the Ni layer to form very large domains, of tens to hundreds of microns,[47] competes with the non-uniform stress caused by the different V_2O_3 phases. Such competition is the reason the Ni domains may resemble the lateral structure of the underlying V_2O_3 domains. Spatially resolved maps of the local SPT transition temperatures were also obtained from the analysis of the Ni domain pattern at each temperature (Fig. 6b). Note that such a spatial distribution of the local transition temperatures cannot be directly inferred from macroscopic measurements, which are subject to statistical averaging. Figure 6b reveals that the temperature at which the induced Ni reversal occurs is a local property of the sample, thus corroborating the spatial phase coexistence across the V_2O_3 SPT. Temperature cycling studies show that different magnetic domains nucleate and grow at different locations following a different detailed evolution (see for comparison Fig. 3 and Fig. S4 in the Supporting Information). Furthermore, there is no obvious relation between the spatial distribution of the SPT temperatures obtained from the Ni domain pattern and the size and shape of the Ni domains themselves. This is a further indication that the nucleation of Ni domains across the SPT is stochastic and therefore not linked to specific V_2O_3 structural grains or defects acting as pinning centres, in agreement with the largely spontaneous positions of the low-temperature/high-temperature V_2O_3 structural phases.[25]

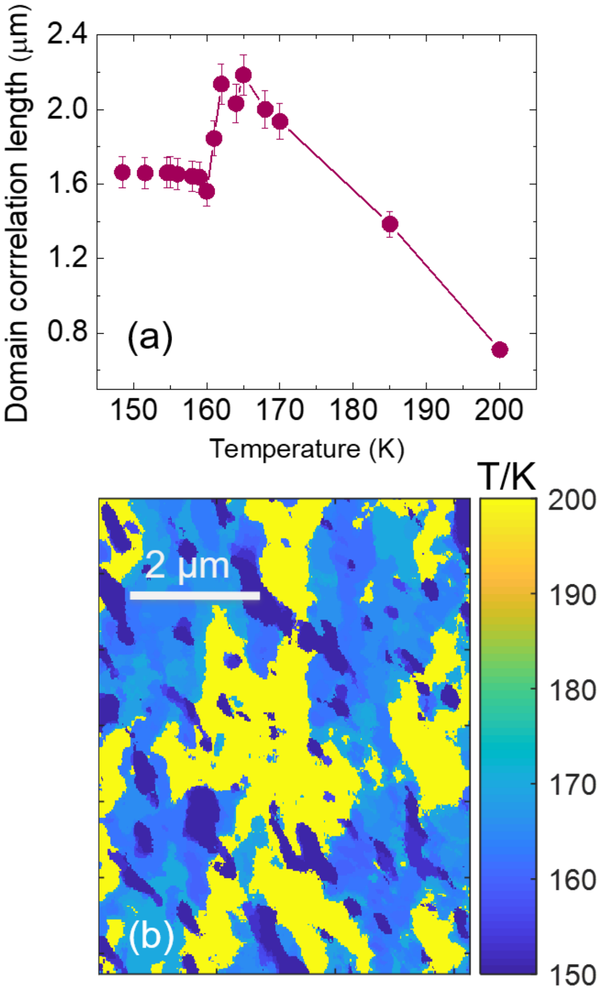

Fig. 6 (a) Domain correlation length for Ni(10 nm)/V_2O_3(100 nm) as a function of the temperature across the V_2O_3 structural phase transition obtained from a pair correlation function analysis of the XMCD images. The correlation lengths are computed by fitting the experimental pair correlation curves to an exponential decay (see also Fig. S6 in the Supporting Information). The correlation length reaches a maximum at the temperature at which the largest phase coexistence is found. (b) Spatially resolved map of local SPT temperatures, obtained from the analysis of the Ni domain pattern at each temperature, corroborating the spatial phase coexistence across the V_2O_3 SPT.

Conclusions

We have used local XMCD imaging as a function of temperature to show that the first-order structural phase transition of V_2O_3 imprints a magnetic domain pattern in a proximity-coupled Ni layer. By characterizing the Ni magnetic domains, we find a bimodal distribution of XMCD intensities and a domain rotation that persists below the SPT. Furthermore, the lateral correlation length of the Ni domains shows a significant increase at the SPT compared to either low- or high- temperature phases, and a broad distribution of the local transition temperatures is found. All the above features point to phase coexistence of Ni magnetic anisotropies induced by interfacial stress transfer with the V_2O_3 across the first-order structural phase transition of the latter. These results are supported by global static (VSM) and dynamic (FMR) magnetometry measurements as well as by micromagnetic simulations. The observed enhanced magnetic response, namely the breaking down of the usual Ni domain pattern and the significant increase of the magnetic anisotropy that give rise to a factor of 4 coercivity increase across a very narrow temperature range, is significantly larger compared with other approaches aiming at the control of magnetism without a magnetic field. Our findings thus provide promising groundwork for novel device concepts based on straintronics.

Conflicts of interest

There are no conflicts to declare.

Acknowledgements

This work was supported by the Spanish MINECO projects MAT2015-68772-P and PGC2018-097789-B-I00 and European Union FEDER funds. A.F.R. and M.G.M acknowledge financial support from the EU CALIPSO Transnational Access programme. J.G.R. acknowledges support from Colciencias under grant 120471250659. The work by I.V., C.W. and I.K.S. at UCSD (synthesis, characterization, magnetization and FMR) were supported by the Office of Basic Energy Science, U.S. Department of Energy, BES-DMS funded by the Department of Energy's Office of Basic Energy Science, DMR under grant DE FG02 87ER-45332.

Notes and references

1 A. Hirohata, K. Yamada, Y. Nakatani, L. Prejbeanu, B. Diény, P. Pirro and B. Hillebrands, *J. Magn. Magn. Mater.*, 2020, **509**, 166711.

2 T. Saerbeck, J. De La Venta, S. Wang, J. G. Ramírez, M. Erekhinsky, I. Valmianski and I. K. Schuller, *J. Mater. Res.*, 2014, **29**, 2353–2365.

3 C. Feng, S. Wang, L. Yin, X. Li, M. Yao, F. Yang, X. Tang, L. Wang, W. Mi and G. Yu, *Adv. Funct. Mater.*, 2018, **28**, 1803335.

4 L. Wang, C. Feng, Y. Li, F. Meng, S. Wang, M. Yao, X. Xu, F. Yang, B. Li and G. Yu, *ACS Appl. Mater. Interfaces*, 2019, **11**, 32475–32480.

5 D. Yi, J. Liu, S. L. Hsu, L. Zhang, Y. Choi, J. W. Kim, Z. Chen, J. D. Clarkson, C. R. Serrao, E. Arenholz, P. J. Ryan, H. Xu, R. J. Birgeneau and R. Ramesh, *Proc. Natl. Acad. Sci. U. S. A.*, 2016, **113**, 6397–6402.

6 C. Feng, Y. Li, L. Wang, Y. Cao, M. Yao, F. Meng, F. Yang, B. Li, K. Wang and G. Yu, *Adv. Funct. Mater.*, 2020, **30**, 1909708.

7 N. A. Spaldin and R. Ramesh, *Nat. Mater.*, 2019, **18**, 203–212.

8 C. Song, B. Cui, F. Li, X. Zhou and F. Pan, *Prog. Mater. Sci.*, 2017, **87**, 33–82.

9 D. Chiba, M. Sawicki, Y. Nishitani, Y. Nakatani, F. Matsukura and H. Ohno, *Nature*, 2008, **455**, 515–518.

10 R. O. Cherifi, V. Ivanovskaya, L. C. Phillips, A. Zobelli, I. C. Infante, E. Jacquet, V. Garcia, S. Fusil, P. R. Briddon, N.

Guiblin, A. Mougin, A. A. Ünal, F. Kronast, S. Valencia, B. Dkhil, A. Barthélémy and M. Bibes, *Nat. Mater.*, 2014, **13**, 345–351.

11 J. T. Heron, J. L. Bosse, Q. He, Y. Gao, M. Trassin, L. Ye, J. D. Clarkson, C. Wang, J. Liu, S. Salahuddin, D. C. Ralph, D. G. Schlom, J. Íñiguez, B. D. Huey and R. Ramesh, *Nature*, 2014, **516**, 370–373.

12 F. Matsukura, Y. Tokura and H. Ohno, *Nat. Nanotechnol.*, 2015, **10**, 209–220.

13 Y. Zhang, W. Xiong, W. Chen, X. Luo, X. Zhang and Y. Zheng, *Phys. Chem. Chem. Phys.*, 2020, **22**, 4685–4691.

14 J. Jeong, N. Aetukuri, T. Graf, T. D. Schladt, M. G. Samant and S. S. P. Parkin, *Science (80-.).*, 2013, **339**, 1402–1406.

15 G. Wei, X. Lin, Z. Si, D. Wang, X. Wang, X. Fan, K. Deng, K. Liu, K. Jiang, N. Lei, Y. Chen, S. Mangin, E. Fullerton and W. Zhao, *Adv. Quantum Technol.*, 2020, **3**, 1900104.

16 J. De La Venta, S. Wang, J. G. Ramirez and I. K. Schuller, *Appl. Phys. Lett.*, 2013, **102**, 1–6.

17 J. De La Venta, S. Wang, T. Saerbeck, J. G. Ramírez, I. Valmianski and I. K. Schuller, *Appl. Phys. Lett.*, 2014, **104**, 062410.

18 D. B. McWhan and J. P. Remeika, *Phys. Rev. B*, 1970, **2**, 3734–3750.

19 P. D. Dernier and M. Marezio, *Phys. Rev. B*, 1970, **2**, 3771–3776.

20 D. B. McWhan, A. Menth, J. P. Remeika, W. F. Brinkman and T. M. Rice, *Phys. Rev. B*, 1973, **7**, 1920–1931.

21 P. Limelette, A. Georges, D. Jérome, P. Wzietek, P. Metcalf and J. M. Honig, *Science (80-.).*, 2003, **302**, 89–92.

22 E. Abreu, S. Wang, J. G. Ramírez, M. Liu, J. Zhang, K. Geng, I. K. Schuller and R. D. Averitt, *Phys. Rev. B*, 2015, **92**, 1–6.

23 E. Abreu, S. N. Gilbert Corder, S. J. Yun, S. Wang, J. G. Ramírez, K. West, J. Zhang, S. Kittiwatanakul, I. K. Schuller, J. Lu, S. A. Wolf, H. T. Kim, M. Liu and R. D. Averitt, *Phys. Rev. B*, 2017, **96**, 1–10.

24 G. Lantz, B. Mansart, D. Grieger, D. Boschetto, N. Nilforoushan, E. Papalazarou, N. Moisan, L. Perfetti, V. L. R. Jacques, D. Le Bolloc'h, C. Laulhé, S. Ravy, J. P. Rueff, T. E. Glover, M. P. Hertlein, Z. Hussain, S. Song, M. Chollet, M. Fabrizio and M. Marsi, *Nat. Commun.*, 2017, **8**, 1–7.

25 A. S. McLeod, E. Van Heumen, J. G. Ramirez, S. Wang, T. Saerbeck, S. Guenon, M. Goldflam, L. Anderegg, P. Kelly, A. Mueller, M. K. Liu, I. K. Schuller and D. N. Basov, *Nat. Phys.*, 2017, **13**, 80–86.

26 F. J. Morin, *Phys. Rev. Lett.*, 1959, **3**, 34–36.

27 M. Imada, A. Fujimori and T. Yoshinori, *Philos. Mag. Lett.*, 1998, **70**, 1039–1263.

28 M. Yethiraj, *J. Solid State Chem.*, 1990, **88**, 53–69.

29 K. Schneider, *J. Mater. Sci. Mater. Electron.*, 2020, **31**, 10478–10488.

30 H. Liu, Z. H. Wang, L. Li, Y. X. Fan and Z. Y. Tao, *Sci. Rep.*, 2019, **9**, 1–10.

31 A. A. Bukharaev, A. K. Zvezdin, A. P. Pyatakov and Y. K. Fetisov, *Uspekhi Fiz. Nauk*, 2018, **188**, 1288–1330.

32 D. A. Gilbert, J. G. Ramírez, T. Saerbeck, J. Trastoy, I. K. Schuller, K. Liu and J. De La Venta, *Sci. Rep.*, 2017, **7**, 1–9.

33 I. Valmianski, J. G. Ramirez, C. Urban, X. Batlle and I. K. Schuller, *Phys. Rev. B*, 2017, **95**, 1–6.

34 F. Kronast, J. Schlichting, F. Radu, S. K. Mishra, T. Noll and H. A. Dürr, *Surf. Interface Anal.*, 2010, **42**, 1532–1536.

35 F. Kronast and S. Valencia Molina, *J. large-scale Res. Facil. JLSRF*, 2016, **2**, 1–6.

36 J. Park and L. Tjeng, *Phys. Rev. B - Condens. Matter Mater. Phys.*, 2000, **61**, 11506–11509.

37 A. Singer, J. G. Ramirez, I. Valmianski, D. Cela, N. Hua, R. Kukreja, J. Wingert, O. Kovalchuk, J. M. Glownia, M. Sikorski, M. Chollet, M. Holt, I. K. Schuller and O. G. Shpyrko, *Phys. Rev. Lett.*, 2018, **120**, 207601.

38 B. D. Cullity C. D. Graham, *Introduction to Magnetiic Materials*, Wiley-IEEE Press, 2008.

39 A. Scholl, H. Ohldag, F. Nolting, J. Stöhr and H. A. Padmore, *Rev. Sci. Instrum.*, 2002, **73**, 1362.

40 J. Stöhr, Y. Wu, B. D. Hermsmeier, M. G. Samant, G. R. Harp, S. Koranda, D. Dunham and B. P. Tonner, *Science (80-.).*, 1993, **259**, 658–661.

41 E. K. H. Salje, *ChemPhysChem*, 2010, **11**, 940–950.

42 J. F. Scott, *NPG Asia Mater.*, 2013, **5**, 1–11.

43 M. J. Donahue and D. G. Porter, *OOMMF User's Guide, Version 1.0*, 1999.

44 R. Skomsk, *J. Phys. Condens. Matter*, 2003, **15**, R841–R896.

45 M. Lange, S. Guénon, Y. Kalcheim, T. Luibrand, N. M. Vargas, D. Schwebius, R. Kleiner, I. K. Schuller and D. Koelle, , DOI:http://arxiv.org/abs/2009.12536.

46 Leo P. Kadanoff, *Rev. Mod. Phys.*, 1967, **39**, 395–431.

47 A. Hubert and R. Schafer, Springer, Berlin, 1998.